ADVANCING EARTH AND SPACE SCIENCES

JGR Solid Earth

RESEARCH ARTICLE
10.1029/2023JB028217

Seasonal Modulation of Crustal Seismicity in Northeastern Japan Driven by Snow Load

Taku Ueda[1], Aitaro Kato[2], Christopher W. Johnson[3], and Toshiko Terakawa[4]

[1]Disaster Prevention Research Institute, Kyoto University, Kyoto, Japan, [2]Earthquake Research Institute, University of Tokyo, Tokyo, Japan, [3]Los Alamos National Laboratory, Los Alamos, NM, USA, [4]Earthquake and Volcano Research Center, Graduate School of Environmental Studies, Nagoya University, Nagoya, Japan

Key Points:

- The spatial distribution of seasonal surface load across northeastern Japan is estimated using Global Navigation Satellite System displacement observations
- The stress amplitude induced by the estimated seasonal surface load modestly modulates the inland seismicity
- This weaker modulation may be due to smaller stress change perturbations and the lower likelihood of unclogging saturated fractures

Supporting Information:

Supporting Information may be found in the online version of this article.

Correspondence to:

T. Ueda,
ueda.taku.2i@kyoto-u.ac.jp

Citation:

Ueda, T., Kato, A., Johnson, C. W., & Terakawa, T. (2024). Seasonal modulation of crustal seismicity in northeastern Japan driven by snow load. *Journal of Geophysical Research: Solid Earth*, *129*, e2023JB028217. https://doi.org/10.1029/2023JB028217

Received 6 NOV 2023
Accepted 19 FEB 2024

Author Contributions:

Conceptualization: Taku Ueda
Formal analysis: Taku Ueda
Funding acquisition: Taku Ueda
Supervision: Aitaro Kato
Visualization: Taku Ueda
Writing – original draft: Taku Ueda
Writing – review & editing: Aitaro Kato, Christopher W. Johnson, Toshiko Terakawa

Abstract Numerous studies have reported that surface hydrological loading can seasonally modulate seismicity rates at crustal depths. For example, substantial winter snow accumulation occurs across the Japanese Islands, and these snowy regions appear to have seasonally modulated the occurrence of previous large inland earthquakes. Therefore, it is important to investigate the impact of seasonal stress changes on crustal seismicity to deepen our understanding of earthquake generation. Here we constrain seasonal changes in the surface load across northeastern Japan using Global Navigation Satellite System surface displacements and evaluate the potential relationship between temporal trends in inland seismicity and estimated seasonal stress changes. The spatial distribution of the seasonal surface load is consistent with snow depth along the Sea of Japan. The inland seismicity beneath northeastern Japan is modestly modulated by the seasonal stress changes that are induced by the annual snow load. However, this seasonal response is weaker than that in other regions. This weak modulation may be due to the small surface-load-induced stress perturbation relative to the long-term-averaged stressing rate and/or the limited presence of crustal fluids to trigger seismicity in Japan.

Plain Language Summary The number of earthquakes can be seasonally controlled by surface processes, such as snow accumulation and melt. Therefore, it is important to estimate the temporal stress changes where earthquakes occur to clarify the role of surface processes in the timing of earthquake occurrence. Here we estimate seasonal changes in surface mass from a dense array of surface displacement observations across northeastern Japan and compare the timing of shallow earthquake occurrence with the stress changes induced by the estimated surface mass. The estimated seasonal surface mass can be explained using snow depth observations along the Sea of Japan. The seasonal stress changes induced by the snow appear to weakly control the number of earthquakes in northeastern Japan. The reason why the number of earthquakes does not vary much seasonally may be because the seasonal stress changes are small compared to the long-term stressing rate.

1. Introduction

Seismicity rates may correlate with natural phenomena at the surface/near surface that produce temporal changes in the local stress field and fault strength, such as hydrological loading (Amos et al., 2014; Bettinelli et al., 2008; Craig et al., 2017; Heki, 2003; Hsu et al., 2021; Johnson et al., 2017a, 2017b, 2020; She et al., 2022; Xue et al., 2020, 2021; Yao et al., 2022), precipitation (Hainzl et al., 2006, 2013), atmospheric pressure changes (Gao et al., 2000), and surface temperature variations (Ben-Zion & Allam, 2013). For example, the seismicity rate in California varies seasonally in response to stress changes related to annual variations in hydrological loading (Amos et al., 2014; Johnson et al., 2017b). Johnson et al. (2017b) calculated the stress changes that hydrological loading imposes on fault planes based on Global Positioning System (GPS) vertical displacements and showed that the seismicity rate in California is more likely to increase when the shear stress increases. Seasonal variations in seismicity rates have also been observed in Japan, and against crustal earthquakes the seasonal snow load and precipitation rate have been suggested as plausible causes (Heki, 2003; M. Okada, 1982; Ueda & Kato, 2019; Xue et al., 2021). Heki (2003) reported that previous large inland earthquakes ($M \geq 7$) in the snowy regions of the Japanese Islands tended to occur more frequently in spring and summer than in fall and winter owing to the spring thaw potentially inducing the unclamping of fault planes. However, few studies have directly compared the seasonal variations in crustal seismicity in Japan with surface-load-induced stress changes.

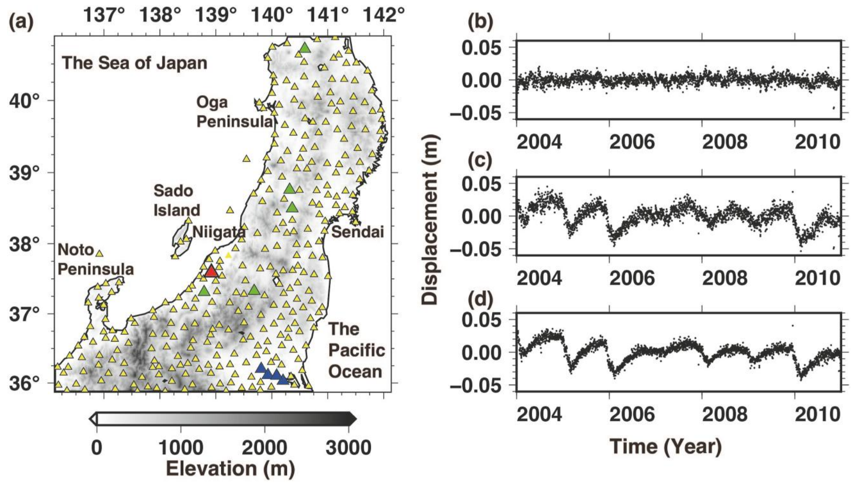

Figure 1. Global Navigation Satellite System (GNSS) station distribution and example vertical-displacement time series. (a) Map of the GNSS Earth Observation Network GNSS station distribution used in this study. Yellow triangles denote the GNSS stations used to estimate seasonal surface loads. The red triangle is station 970810, which is a representative example used in Figures 1 and 2, and Figure S6 in Supporting Information S1. Blue triangles denote stations whose displacement signals were closely related to groundwater-level changes due to local irrigation. Green triangles denote stations whose displacement signals suffered from extremely high seasonal amplitudes. The intensity of the gray color explains elevation taken from ETOPO (NOAA National Centers for Environmental Information, 2022). (b) Time series of common-mode errors (CMEs) for vertical displacements, which were estimated using stations distributed across southern Japan (cyan triangles in Figure S1 in Supporting Information S1). Time series of (c) raw and (d) CME-corrected vertical displacement at station 970810 (red triangle in (a)).

Heavy snow accumulates on the western flanks of the mountain ranges in northeastern Japan during the winter months, and this snow loading generates annual displacements that are observable at local GPS sites (Heki, 2001). Here, we estimate the monthly seasonal surface load using long-term Global Navigation Satellite System (GNSS) surface displacements and comprehensively evaluate the temporal trends in inland seismicity with the estimated seasonal stress perturbations that are resolved on the nodal planes of typical fault mechanisms.

2. Estimation of the Spatiotemporal Surface-Load Distribution

2.1. GNSS and Snow Data

We use the final solutions of the GNSS Earth Observation Network (GEONET) daily coordinates, which are also known as the F5 solutions (Takamatsu et al., 2023), that were determined for the 2004–2010 period (Figure 1) when the number of stations becomes sufficiently large and has little temporal variation and the data is not affected by the 2011 Tohoku-Oki earthquake. We only use the vertical displacements, which are more sensitive to the surface load than the horizontal displacements, to estimate the seasonal surface load.

Maximum snow depth estimates from the AMeDAS (Automatic Meteorological Data Acquisition System) sites determined for the 2004–2010 period are used for comparison with the estimated seasonal surface load.

2.2. Vertical GNSS Time Series and Surface-Load Modeling

The raw GEONET time series contains common-mode noise at all stations, and this noise may obscure the appropriate seasonal displacement variations. We remove the common-mode errors (CMEs) using a procedure that employs principal component analysis (PCA)-based spatiotemporal filtering (Dong et al., 2006). First, we remove the sudden displacements caused by $M_j \geq 6.0$ (M_j; Japan Meteorological Agency [JMA] magnitude) earthquakes that occur within a distance R (km) at which displacement U of 1 cm or more is expected (Y. Okada, 1995):

$$R \leq 10^{\frac{(1.5M_j - \log_{10} U - 6.0)}{2}}. \quad (1)$$

If the distance between the hypocenter and station is within R, we estimate the displacement using the step function and remove it. Furthermore, we estimate any sudden displacements that occurred during antenna replacements (dates are published by GSI) using the step function and remove them. We adopt PCA to a matrix X, whereby each column contains the detrended and demeaned vertical displacements from a single station (x_j), and the rows contain the displacements for all stations at a given epoch (t_i). The matrix X is decomposed by:

$$X(t_i, x_j) = \sum_{k=1}^{n} a_k(t_i)\, v_k(x_j), \tag{2}$$

where $a_k(t)$ is the k th principal component, which represents the temporal variations, and $v_k(x)$ contains the eigenvectors, which represent the corresponding spatial responses to the principal components. We define the first principal component, which is the most spatially uniform mode, multiplied by the median of $v_1(x)$ as the CME.

We use the GNSS stations in southern Japan (cyan triangles in Figure S1 in Supporting Information S1), where it rarely snows, to estimate CME. This station selection can prevent containing snow signals as CME. The estimated CME time series is shown in Figure 1b, and example raw and CME-corrected displacement time series are shown in Figures 1c and 1d, respectively. The CME-corrected data are used to extract seasonal variations via the Greedy Automatic Signal Decomposition algorithm (Figure 2) (Bedford & Bevis, 2018). We assume that the vertical-displacement time series can be expressed in the following form:

$$\begin{aligned} x(t) =& mt + d + \sum_{k=1}^{n_k}\left[s_k \sin(\omega_k t) + c_k \cos(\omega_k t)\right] + \sum_{j=1}^{n_j} b_j H(t - t_j) \\ &+ \sum_{r=1}^{n_r}\sum_{i=1}^{n_i}\left[A_i\left(1 - e^{\left(-\frac{(t-t_r)}{T_i}\right)}\right)\right] + \xi(t), \end{aligned} \tag{3}$$

The first and second terms are secular terms. The third term is the seasonal component, which is expressed as the summation of the annual and semiannual variations. The fourth term is a step function that captures the signals due to earthquakes and equipment repairs. The fifth term represents transient signals, such as slow slip and postseismic deformation. The sixth term is the residual error. We fit Equation 3 to the CME-corrected vertical displacement time series (e.g., Figure 1d) without assuming the timing and number of any step or transient changes (Bedford & Bevis, 2018).

We select the seasonal vertical displacements (e.g., Figure 2d) extracted from 303 stations (yellow triangles in Figure 1a) to estimate the monthly change in seasonal surface load averaged during 2004–2010. We exclude the vertical displacements from 10 stations in this analysis because the displacements at five stations are closely related to groundwater-level changes due to local irrigation (blue triangles in Figure 1a; Munekane et al., 2004; Tobita et al., 2004) and the displacements at another five stations contain high seasonal amplitudes which are more than three standard deviation larger than the average of the seasonal amplitudes of the yellow and green stations (green triangles in Figure 1a). These high amplitudes are interpreted as possibly due to the groundwater extraction for snow melting (e.g., Shimada et al., 2021) or more snow locally than in the surrounding area, and do not reflect the appropriate amount of snow at that location.

The extracted seasonal components of the vertical displacements are inverted to obtain the monthly change in the seasonal surface load as a function of location (Figure S2 in Supporting Information S1) by simultaneously minimizing the misfit of the model to the data, a Laplacian term that constrains the spatial variations in the surface load between neighboring grid points, and a damping term that limits the surface-load changes. The change in the surface loads are estimated at 0.25° intervals (latitude and longitude). The Green's function of the vertical displacements s_{up} (m) at Earth's surface represents a circular disc load (1 kg/m^2) with an angular radius α (°), which takes the following form (Wahr et al., 2013):

$$s_{up} = \sum_{n=0}^{\infty} h_n \Gamma_n \frac{4\pi G a}{g(2n+1)} P_n(\cos\theta), \tag{4}$$

10.1029/2023JB028217

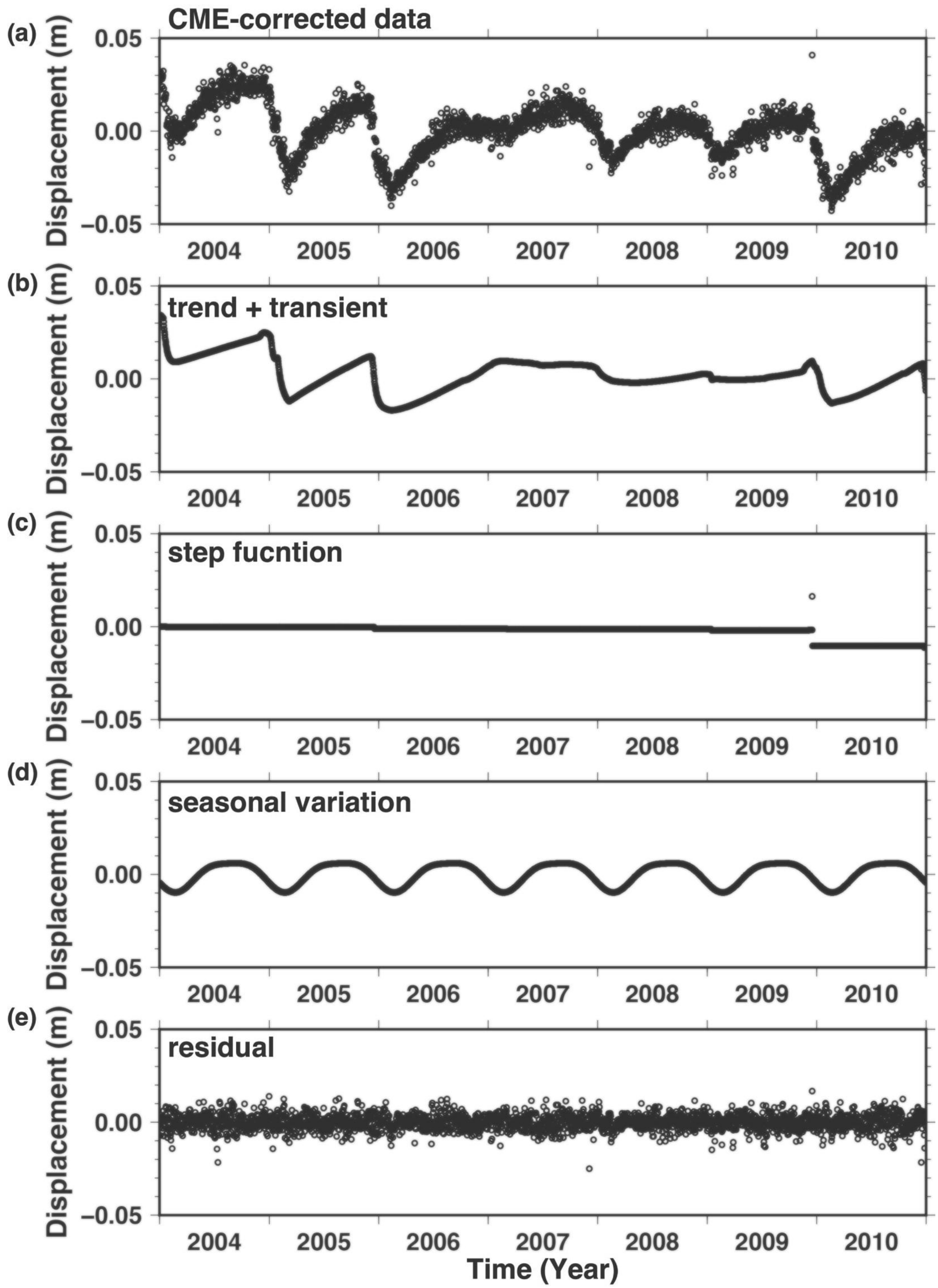

Figure 2. Decomposition of the vertical-displacement time series. (a) CME-corrected vertical displacements at station 970810 (red triangle in Figure 1; same figure as Figure 1d). (b) Trend and transient component, (c) step component, (d) seasonal component, and (e) residual of the CME-corrected vertical displacement in (a), with each component extracted via the approach in Bedford and Bevis (2018).

where:

$$\Gamma_n = \frac{1}{2}[P_{n-1}(\cos\alpha) - P_{n+1}(\cos\alpha)] \text{ for } n > 0, \Gamma_0 = \frac{1}{2}(1 - \cos\alpha), \tag{5}$$

10.1029/2023JB028217

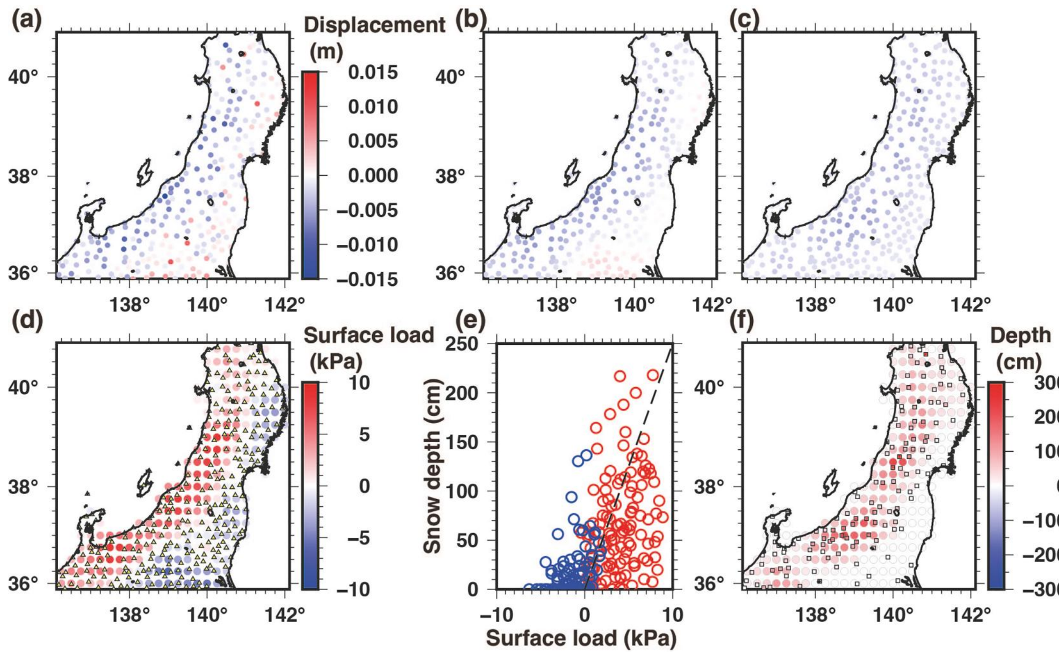

Figure 3. Spatial distributions of vertical displacements, surface load, and maximum snow depth across the study area. (a) Extracted seasonal component of the vertical displacements in mid-March (relative to mid-August). (b) Calculated vertical displacements using the spatial distribution of surface load in (d). (c) Expected vertical displacements using the observed snow load, which was derived from the averaged maximum snow depth in (f). (d) Spatial distribution of surface load, which was estimated from the displacements in (a). (e) Relationship between the estimated surface load in (d) and averaged maximum snow depth in (f) for every grid point in the model. Red and blue points are the data in the Sea of Japan region and the Pacific Coast region, respectively. The dashed line shows the theoretical relationship between snow depth and surface load using a snow density of 400 kg/m^3. (f) Averaged maximum snow depth data for March based on the AMeDAS site observations (black squares).

h_n contains the load Love numbers, which are calculated using the approach in Wang et al. (2012) based on the Preliminary Reference Earth Model (PREM; Dziewonski & Anderson, 1981), G is Newton's gravitational constant, a is Earth's radius, g is the gravitational acceleration at Earth's surface, θ is the angular distance away from the center of the disc load, and P_n is the Legendre function. The PREM might be too simple, but it is assumed that structural heterogeneity at shorter wavelengths does not have much effect because the surface load model in this study is based on a spatial scale of about 0.25°. We set the angular radius α to 0.125°, then minimize the misfit function as follows:

$$\|\boldsymbol{w}(\boldsymbol{Gm}-\boldsymbol{d})\|^2 + {\lambda_1}^2\|\boldsymbol{Lm}\|^2 + {\lambda_2}^2\|\boldsymbol{m}\|^2, \tag{6}$$

where $\boldsymbol{d}$ is the data vector, which contains the extracted seasonal component from the observed GNSS vertical displacements, $\boldsymbol{w}$ is a weighting matrix ($w_{ij} = \delta_{ij}/\sigma_i$, where σ_i is the root-mean-square amplitude of the residual term of each station, Equation 3), $\boldsymbol{m}$ is the model vector, which contains the model surface load at each grid point, $\boldsymbol{G}$ is the matrix consisting of Green's functions (Equation 4), and $\boldsymbol{L}$ is the Laplacian operator. We employ a grid search scheme to the estimated λ_1 and λ_2 values that minimize Akaike's Bayesian Information Criterion (ABIC; Akaike, 1980), following Fukahata et al. (2004).

2.3. Surface-Load Results

The spatial distribution of the vertical displacements in mid-March relative to mid-August is shown in Figure 3a. The spatial distribution of the surface load changes in Figure 3d is estimated using these displacements (Figure 3a), with ~0.5° (latitude and longitude) spatial smoothing applied. An increase in load is estimated in areas of subsidence, and a decrease in load is estimated in areas of uplift. Furthermore, areas with an increase in load (Figure 3d) are spatially coincident with the snowy region (Figure 3f).

10.1029/2023JB028217

The dependence of λ_1 and λ_2 in Equation 6 on ABIC of the surface-load models is shown in Figure S3 in Supporting Information S1. The difference in ABIC from the best (smallest ABIC) model (ΔABIC) indicates that exp(−ΔABIC/2) can be interpreted as the relative probability of a given model fit compared with the best model (Akaike, 1980; Kumazawa & Ogata, 2013). Therefore, models with ΔABIC < 6 can be accepted with a probability of >5%. The spatially roughest and smoothest surface-load models with ΔABIC < 6 are shown in Figures S4a and S4b in Supporting Information S1, respectively. The spatial distributions of the two models are similar to that of the best model (Figure 3d), which suggests that the best model provides a robust estimate of the surface-load distribution.

The spatial distributions of the monthly change in estimated surface load during 2004–2010 are shown in Figure 4. There is a large amount of snow cover from November to January along the Sea of Japan, with the associated increase in load (average of 1.37 ± 0.95 kPa) showing subsidence during the winter season (Figures 4a, 4k, and 4l). Conversely, a decrease in load is estimated from March to May (Figures 4c–4e) as the snow melts, thereby reducing the average load to −1.29 ± 0.98 kPa. The estimated surface load change fluctuates around zero from June to October (average of 0.01 ± 0.66 kPa; Figures 4f–4j), when the region is snow free. The opposite trend is generally observed in the monthly change in estimated surface loads along the Pacific Ocean, but with lower amplitudes. This trend along the Pacific Ocean is inconsistent with the increase in surface load due to snowfall during the winter season.

2.4. Surface-Load Evaluation

Our results reveal that the increase in surface loads (Figure 3d) correspond to the snowy region in northeastern Japan (Figure 3f). We demonstrate that the snow load is a plausible source of the subsidence by comparing the spatial distribution of the estimated surface load (Figure 3d), which was derived from the observed vertical displacements (Figure 3a), with the spatial distribution of the snow load by spatially smoothing the observed averaged maximum snow depth data for March at the AMeDAS sites (Figure 3f). There is a positive correlation between the estimated surface load and observed snow depth when a snow density of 400 kg/m^3 is assumed, as shown in Figure 3e.

We also calculate the expected vertical displacement at each GNSS station (Figure 3c) based on the Green's functions (Equation 4), whereby we use the averaged maximum snow depth (Figure 3f) and an assumed snow density of 400 kg/m^3 to calculate the observed snow load. The spatial distribution of the expected vertical displacement (Figure 3c) roughly corresponds to the amplitude of the observed subsidence at the GNSS stations (Figure 3a) along the Sea of Japan. However, the maximum subsidence (~6 mm) that is expected from the snow depth is less than the maximum observed GNSS vertical displacement (~15 mm). There are two main possible causes of this discrepancy. One is the uncertainty of the snow depth, the snow density, and the GNSS vertical displacement. AMeDAS stations are often located at inhabitable elevations rather than in mountain areas where it is difficult to maintain observations and it has much snow (Heki, 2004). Heki (2004) also noted that snow density increases toward the end of winter. Thus, the snow depth observed by AMeDAS and the assumed density of snow possibly underestimate the subsidence. GNSS displacement measurements may also be incorrect because of snow accretion on the GNSS pillar and/or radome covering the antenna, thereby impeding the GNSS signals and enhancing signal scattering effects (Jaldehag et al., 1996). Another possible cause is that the observed GNSS subsidence includes loading sources other than the snow mass, which is obtained from the snow depth. For example, atmospheric load also affects the seasonal variations in displacement (Heki, 2004). We calculate the vertical displacement in March relative to August caused by non-tidal atmospheric loading (NTAL) using the data in spherical harmonics provided by GFZ German Research Center for Geosciences (GRACE, 2018) and Equation 4 of Zhang et al. (2021). We correct the vertical displacement (Figure S5a in Supporting Information S1) by subtracting the displacement caused by NTAL and reestimate spatial variations in surface load (Figure S5b in Supporting Information S1). The contribution of NTAL is <0.5 mm in displacement and <0.8 kPa in estimated surface load. Thus, the atmospheric load is too small to explain the discrepancy between observed vertical displacements and expected displacements due to snow. Geodetic investigations of groundwater from snow melt along roads in the Niigata area have also indicated significant subsidence (Morishita et al., 2020; Sato et al., 2003; Shimada et al., 2021). Additionally, the impoundment of dams might affect vertical displacement, but its contribution is much less than snow and atmosphere (Heki, 2004). Other sources of this uncertainty may be the regularization of the current inversion scheme, which smooths the surface-load model and makes it less sensitive to the data variability. Although factors other than snow load may contribute to the observed vertical

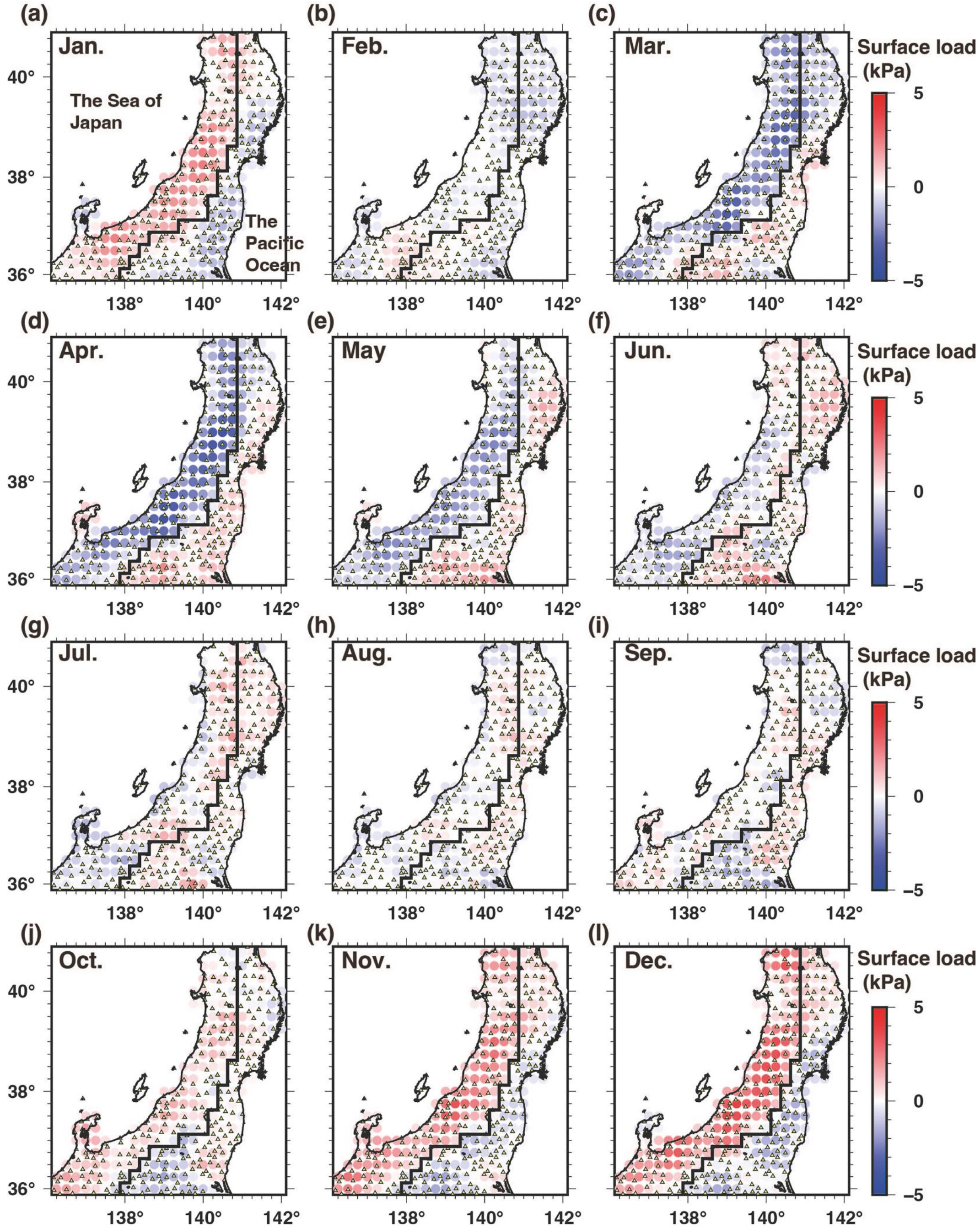

Figure 4. Spatial distribution of monthly change in surface load, estimated using the seasonal component extracted from the vertical displacements. The black line marks the boundary between the area along the Sea of Japan and the area along the Pacific Ocean.

displacement, we conclude that snow load is a plausible cause of the seasonal variations in vertical displacements along the eastern margin of the Sea of Japan.

The seasonal component of the vertical displacement along the Pacific Ocean in March relative to August shows signal consistent with uplift (Figure 3a), and a corresponding negative surface load is estimated (Figure 3d). Although this result is inconsistent with snow accumulation in winter, the uplift in March has been confirmed by Fujiwara et al. (2022), who extracted the averaged displacement in March after the 2011 Tohoku-Oki earthquake.

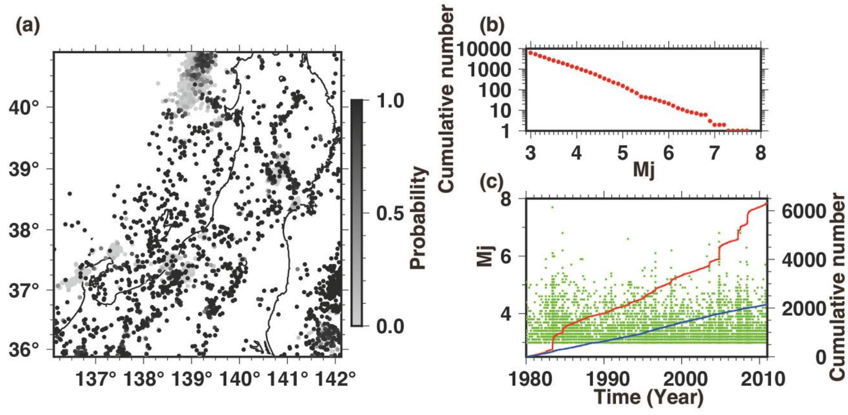

Figure 5. Earthquake data used in this study. (a) Epicenter distribution ($M_j \geq 3.0$). The intensity of the gray color indicates the probability a given event is a background earthquake by applying the Hierarchical Space-Time Epidemic-Type Aftershock Sequence model (e.g., Ogata, 2004). (b) Cumulative frequency–magnitude distribution. (c) Magnitude–time plot (green circles). Red and blue lines denote the cumulative numbers of total earthquakes and background earthquakes, respectively.

The observed uplift along the Pacific Ocean is considered a true signal; however, it is uncertain whether this signal can be interpreted as deformation owing to changes in the surface load. We discuss the contribution of the changes in surface load along the Pacific Ocean margin in Section 3.4 to evaluate the relationship between surface-load-induced stress changes and temporal trends in inland seismicity.

In this study, we extract the averaged seasonal component during the 2004–2010 period (Figure 2d). We observe that the magnitude of the subsidence increases as more snow accumulates or more groundwater extraction for snow melting across the region (Figure S6 in Supporting Information S1). The transient component (Figure 2b) may explain year-to-year changes that cannot be explained by averaged seasonal variation. We note that any seasonal changes in the time-varying amplitudes (Cleveland et al., 1990; Köhne et al., 2023) should be examined in a future study. Furthermore, careful consideration must be taken to exclude the effects of both groundwater (Morishita et al., 2020; Sato et al., 2003; Shimada et al., 2021) and snow accretion on the GPS antenna (Heki & Jin, 2023; Larson, 2013; Larson et al., 2015) from the vertical displacements when estimating the spatiotemporal distribution of the surface load. Note that Heki and Jin (2023) proposed a method to discriminate fake signals due to snow accretion from real subsidence.

3. Evaluation of Temporal Trends in Inland Seismicity and Resolved Stress Perturbations

3.1. Earthquake Catalog Data

The earthquake data in our analysis are taken from the JMA hypocenter catalog (Figure 5). We use $M_j \geq 3.0$ shallow crustal earthquakes (≤25 km depth) that occurred during 1980–2010. We confirm that the $M_j \geq 3.0$ earthquakes are almost completely detected based on the obtained goodness of fit to Gutenburg–Richter law of >90 (Figure 5b) (Wiemer & Wyss, 2000).

Aftershocks should be removed via a declustering technique prior to investigating the seasonal modulation of seismicity. Here we apply the Hierarchical Space-Time Epidemic-Type Aftershock Sequence (HIST-ETAS) model (Ogata, 2004; Ogata et al., 2003; Ueda et al., 2021) to the earthquake catalog and the probability that each event is a background event is used as the declustered catalog (Ueda & Kato, 2023; Zhuang et al., 2002). A comparison of the cumulative numbers of total and background earthquakes (Figure 5c) shows that the aftershocks are successfully removed from the original earthquake catalog by the HIST-ETAS model.

We used earthquakes only beneath the given stress field shown in Figure 6 to obtain the seasonal variations in seismicity. Earthquakes outside the stress field are used for appropriate evaluation of the probability for earthquakes beneath the stress field to be a background event.

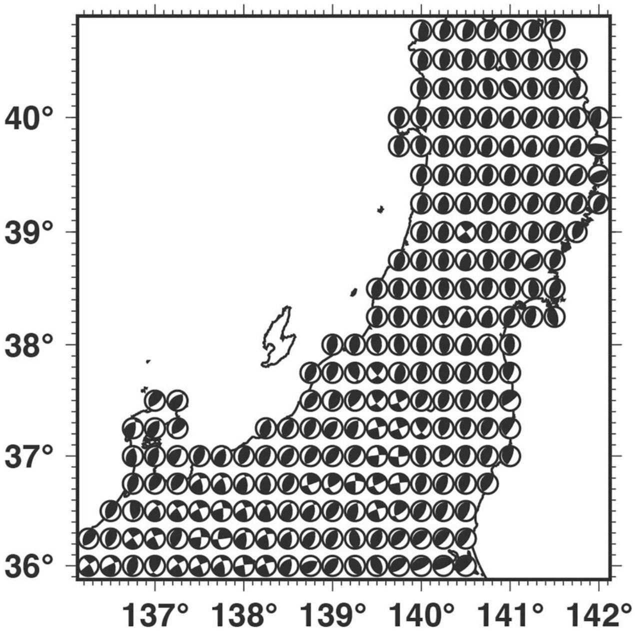

Figure 6. Spatial distribution of planes of maximum shear stress in the tectonic stress field (Terakawa & Matsu'ura, 2008, 2010).

3.2. Seasonal Modulation of Inland Seismicity

We focus on the spatial distribution of the monthly change in surface load (Figure 4), which was derived from the vertical displacements (Section 2.2), to evaluate the relationship between the seasonal surface-load-induced stress changes and the temporal trends in inland seismicity. We employ the approach in Johnson et al. (2017b), whereby we calculate the strain rate tensors using a modified version of STATIC 1D (Pollitz, 1996) that is adapted for a vertical force at the surface (Pollitz et al., 2013) and an assumed PREM structure (Dziewonski & Anderson, 1981). The strain rate tensors are calculated at 10 km depth, which is considered a representative seismogenic depth for the study area. We then convert the strain rate tensors to stress rate tensors by assuming isotropic elasticity with a Poisson ratio of 0.25 and a shear modulus of 35 GPa. We calculate the shear, normal (unclamping is positive), and Coulomb stressing rate (for friction coefficients $\mu = 0.1$, 0.4, and 0.7) on the two planes of maximum shear stress (the two nodal planes where the shear stress is at a maximum in the tectonic stress field) (Figure 6; Terakawa & Matsu'ura, 2008, 2010) at 0.05° intervals (latitude and longitude). We compute the seasonal stress changes by integrating the calculated seasonal stressing rates. The spatial distribution of the monthly Coulomb stressing rates and monthly Coulomb stress changes ($\mu = 0.4$) are shown in Figures 7 and 8, respectively.

We evaluate the temporal trends in inland seismicity with respect to the seasonal surface-load-induced stressing rate/stress changes based on the percentage of excess earthquakes that occurred during a range of stress intervals (Cochran et al., 2004; Johnson et al., 2017a, 2017b, 2020; She et al., 2022; Xue et al., 2021). The percentage of excess earthquakes is calculated according to the following equation:

$$N_{\mathrm{Ex}} = \frac{(N_{\mathrm{Act}} - N_{\mathrm{Exp}})}{N_{\mathrm{Exp}}} \times 100\%, \tag{7}$$

where N_{Ex} is the percentage of excess earthquakes per stress interval, N_{Act} is the actual number of events per stress interval, and N_{Exp} is the expected number of earthquakes under the assumption of a temporally uniform distribution. If the seismicity is modulated by stress and/or stressing rate, N_{Ex} is expected to be positive at positive stress and/or positive stressing rate. The number of earthquakes beneath the region where we estimated the surface load is weighted by the probability that each event is a background event to remove the effect of aftershocks (Figure 5a). We assume that each earthquake is driven by either of the two planes of maximum shear stress at the nearest calculated grid point. We obtain N_{Act} by first randomly selecting one of the two nodal planes (Figure 6) and then adopting the values of stress change or stressing rate in the month when an earthquake occurs. We obtain N_{Exp} by first randomly selecting one of the two nodal planes (Figure 6) and then randomly selecting the values of stress changes or stressing rates from among the 12 months (Figures 7 and 8, respectively). In other words, each earthquake is counted at what stress (or stressing rate) interval it occurred in the above procedure. The stresses and stressing rates are binned in 1.0 and 6.0 kPa/year intervals, respectively. The stress and stressing rate intervals are limited to the 99th percentile of the data range. All stresses and stressing rates outside this range are binned in the outermost stress and stressing rate intervals. We calculate N_{Ex} (Equation 7) and its standard deviation by making a total of 500 N_{Act} and N_{Exp} samples.

3.3. Stress Modulation of Inland Seismicity

The relationships between excess seismicity and stressing rates and stresses induced by the monthly seasonal surface-load distributions (Figure 4) are shown in Figures 9 and 10, respectively. The percent excess seismicity possesses positive correlations with both the Coulomb stressing rate and Coulomb stress changes. The correlation between excess seismicity and stress changes (Figure 10) is more stable than that between excess seismicity and stressing rates (e.g., weak negative correlation with the shear stressing rate (Figure 9b)). The

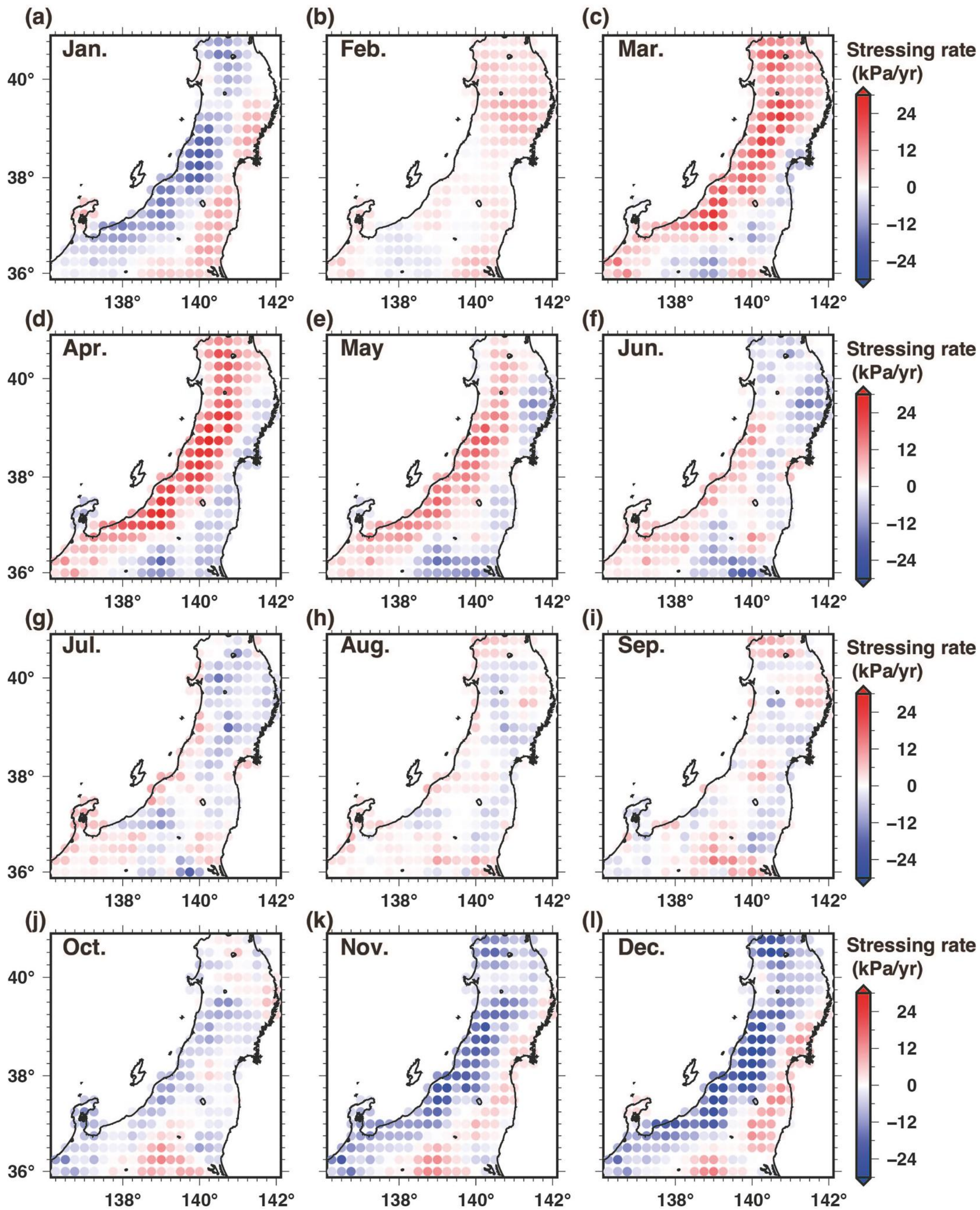

Figure 7. Spatial distributions of the monthly Coulomb stressing rates ($\mu = 0.4$) on the planes of maximum shear stress at 10 km depth induced by the seasonal surface load.

slopes of the percent excess seismicity to the stressing rate and stress are ~0.4 N_{Ex}/(kPa/year) and ~3 N_{Ex}/kPa, respectively. However, these positive correlations are insignificant considering uncertainties (The slopes are possibly zero in some cases.). The relationship between the percent excess seismicity and seasonal surface-load-induced stressing rate/stress has been explored in California (Johnson et al., 2017a, 2017b), Alaska (Johnson et al., 2020), and the Lake Biwa region (Xue et al., 2021). The slopes of the percent excess seismicity to the stressing rate and stress in the inland Tohoku region are smaller than or comparable to those in other studies (2–5 N_{Ex}/[kPa/year] (Xue et al., 2021), >3 N_{Ex}/kPa (Johnson et al., 2017b)), which suggests that the seismicity in the inland Tohoku region is less sensitive to the surface-load-induced stress changes compared with that in other regions.

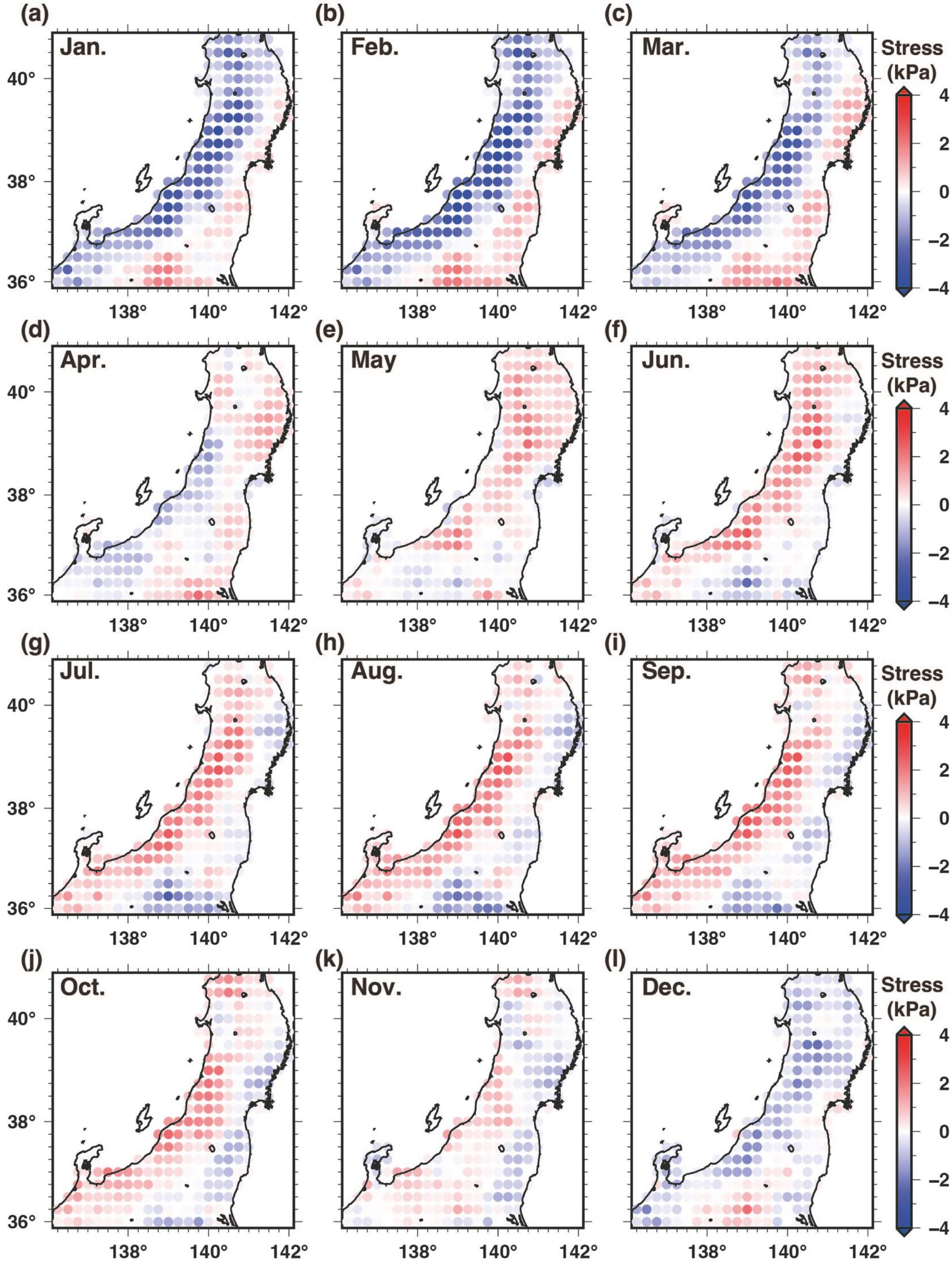

Figure 8. Spatial distributions of monthly Coulomb stress changes ($\mu = 0.4$) on the planes of maximum shear stress at 10 km depth induced by the seasonal surface load.

3.4. Discussion

We calculate the seasonal stress changes using the surface load (Figure 4), which is estimated from the seasonal component of the vertical displacement. However, it is unclear whether the seasonal variations in vertical displacements along the Pacific side of northeastern Japan reflect surface-load changes because they are inconsistent with the snow-load trend, as mentioned in Sections 2.3 and 2.4. Therefore, we evaluate the relationships between

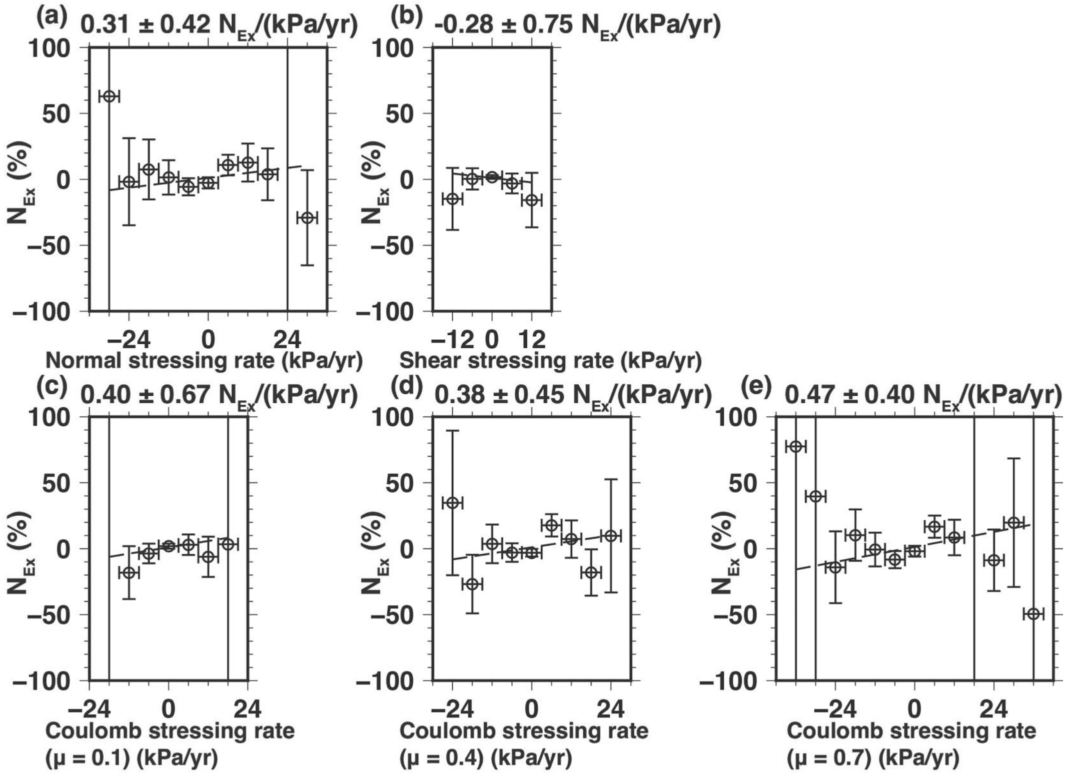

Figure 9. Relationships between excess seismicity and stressing rates. Percent excess seismicity for the (a) normal stressing rate, (b) shear stressing rate, and Coulomb stressing rates for (c) $\mu = 0.1$, (d) $\mu = 0.4$, and (e) $\mu = 0.7$. The bin interval is 6 kPa/year. Error bars show 1σ standard deviation. The dashed lines indicate the best-fit line estimated using the weighted least squares method. The slope of the best-fit line and its 1σ standard deviation are shown above each panel. The positive slope is expected if seismicity is modulated by each kind of stressing rate.

the percent excess seismicity and calculated stressing rate and stress changes using the spatial distribution of the surface load along only the Sea of Japan side of northeastern Japan (Figures S7 and S8 in Supporting Information S1, respectively). We do not identify a correlation between the percent excess seismicity and stressing rates/stress changes beyond the standard deviation, which suggests that the surface-load changes on the Pacific side may be important in modulating inland seismicity. The mechanism(s) for these surface-load changes should be considered in future studies.

Here we assume that the seasonal surface load is the primary factor that modulates the seasonal variations in inland seismicity and investigate the relationship between inland seismicity and surface-load-induced stresses. However, there are other possible mechanisms, such as heavy precipitation infiltration, atmospheric pressure changes, and surface temperature variations (e.g., Ben-Zion & Allam, 2013; Hainzl et al., 2013; Johnson et al., 2017b). Therefore, we also evaluate the effect of ocean loading, which is excited by interactions between surface winds, atmospheric pressure, temperature and density gradients, and currents (Dong et al., 2002). We use the Equivalent Water Height data derived from Gravity Recovery and Climate Experiment (GRACE) and GRACE-Follow-On (FO) and processed at Jet Propulsion Laboratory using the Mascon approach (Wiese et al., 2023) to evaluate ocean loading. We convert the monthly changes in the equivalent water height at the ocean to ocean mass loads by multiplying the heights by the density of water (1,000 kg/m^3). The ocean mass load is discretized on a 0.25° grid (latitude and longitude), and the stressing rate and stress change on the nodal planes induced by the seasonal ocean mass load are calculated using the method in Section 3.2. The relationships between the percent excess seismicity and stressing rates and stresses caused by the summation of terrestrial surface load (Figure 4) and ocean mass load are shown in Figures S9 and S10 in Supporting Information S1, respectively. The positive correlations between the seismicity and stressing rates/stress are still visible, even when the effect of the ocean mass load is considered.

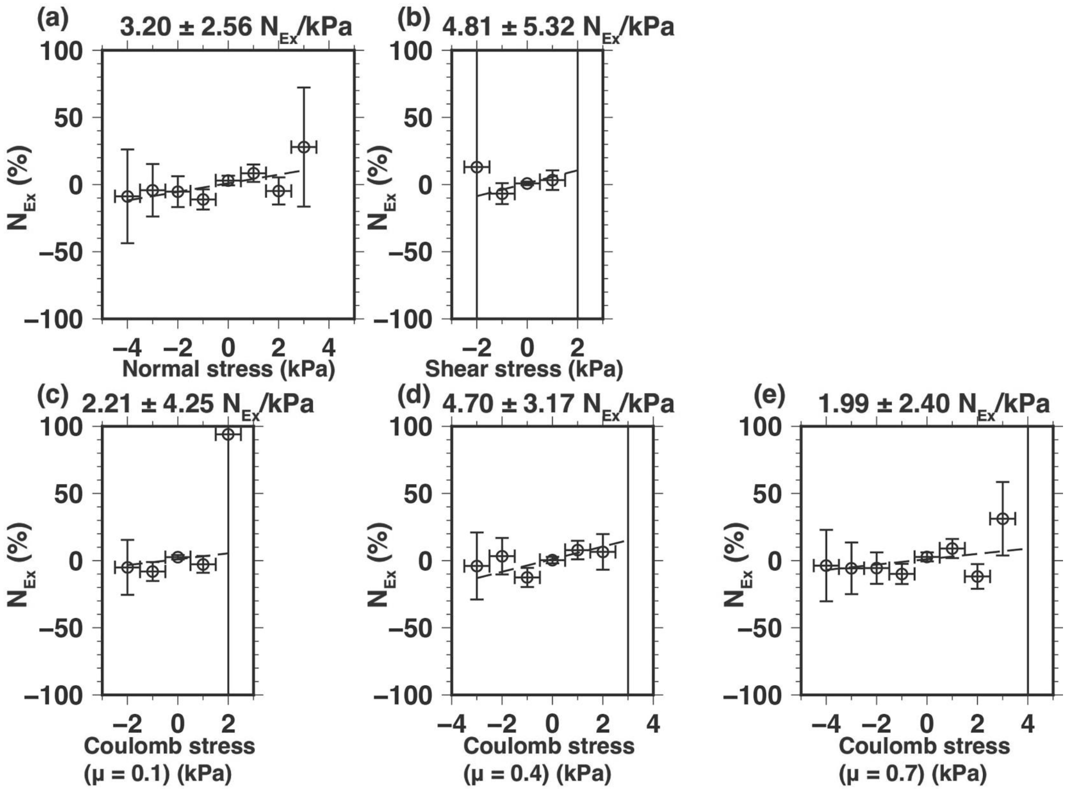

Figure 10. Relationships between the excess seismicity and stresses. Percent excess seismicity for the (a) normal stress, (b) shear stress, and Coulomb stresses for (c) $\mu = 0.1$, (d) $\mu = 0.4$, and (e) $\mu = 0.7$. The bin interval is 1 kPa. The error bars show the 1σ standard deviation. The dashed lines indicate the best-fit line estimated using the weighted least squares method. The slope of the best-fit line and its 1σ standard deviation are shown above each panel. The positive slope is expected if seismicity is modulated by each kind of stress.

Johnson et al. (2017b) evaluated the stresses caused by various types of loading sources, such as hydrological loads, atmospheric pressure changes, temperature variations, and Earth pole tides, and concluded that hydrological loads are the largest source of seasonal stresses in California. The stresses induced by the seasonal surface load and ocean mass load in the present study are comparable to those induced by the estimated hydrological load and ocean mass load in California (Johnson et al., 2017b). Therefore, the hydrological load is likely to be the largest source of seasonal stress, even in Japan; however, additional research is required to verify the importance of the hydrological load on the seasonal stresses in Japan.

We find that the seismicity ($M \geq 3.0$) in the inland Tohoku region is modestly modulated by the surface-load-induced seasonal stressing rate/stresses (Figures 9 and 10). Heki (2003) reported that the historical large earthquakes ($M \geq 7.0$) in snowy region occurred more frequently in spring and summer than in fall and winter, whereas the bimonthly distribution of moderate earthquakes ($6.0 \leq M \leq 7.0$) in the snowy region did not show a clear seasonal variation. However, the location accuracies of the epicenters of historical earthquakes along the Sea of Japan are low, such that these earthquakes may not have truly occurred beneath the snowy region owing to limited information on the associated seismic damage in historical documents. Furthermore, Heki (2003) did not quantitatively evaluate the relationship between the temporal trends in inland seismicity and snow-load-induced stress changes. We identify a positive correlation between the excess seismicity and snow-load-induced stress changes, which supports the idea that large earthquakes are also seasonally modulated by snow load (Heki, 2003). Therefore, the seasonal variability in seismicity in the inland Tohoku region may be a scale-invariant phenomenon. This phenomenon has also been observed in San-in district, southwest Japan (Ueda & Kato, 2019) and California (Johnson et al., 2017a). Note that the sensitivity to seasonal modulation against earthquake magnitude might be different due to the differences in spatial scale for phenomena causing seasonal variations.

We directly compare the number of earthquakes with corresponding seasonal stress changes and stressing rate to evaluate the seasonal modulation of seismicity (Figures 9 and 10). Another method for verifying seasonal variation is to evaluate statistical significance by focusing on which phase angle of the seasonal stress the earthquake occurred (e.g., Tsuruoka et al., 1995). For reference, we perform the Schuster test (Schuster, 1897) assuming that we assign a phase angle of 0° to the peak month of seasonal stress or stressing rate depending on each place, but we couldn't find any statistically significant results for the cases against normal, shear, Coulomb stress and corresponding stressing rate ($p > 50\%$). These results is consistent with insiginificant positive correlation between the excess seismicity and stress (stressing rate), suggesting that seasonal modulation of seismicity in northeastern Japan is very modest.

In this study, we investigate the relationship between the seismicity and both stress and stressing rate. According to laboratory experiments and numerical simulations in 2-D continuum model of a rate-and-state fault, seismicity rate correlates with periodic stressing rate when the period of oscillating stress is longer than the characteristic time corresponding to the duration of nucleation, while seismicity rate correlates with periodic stress when the period of oscillating stress is shorter than characteristic time (Ader et al., 2014; Beeler & Lockner, 2003). Our results indicate that the correlation between excess seismicity and stress changes (Figure 10) is more stable than that between excess seismicity and stressing rates (Figure 9). It refers that the nucleation time of earthquakes with $M_j \geq 3.0$ may be comparable to or longer than a year, consistent with that on the San Andreas System suggested by Beeler and Lockner (2003) and that potentially explaining seasonal variations in Nepal seismicity (Ader et al., 2014). This long nucleation time might explain the reason why earthquake occurrence does not correlate well with semidiurnal or diurnal tides although their amplitude is larger than seasonal variations (Beeler & Lockner, 2003).

Our results (~0.4 N_{Ex}/[kPa/year] and ~3 N_{Ex}/kPa; Figures 9 and 10) suggest that seismicity in the inland Tohoku region is less sensitive to surface-load-induced stress changes than that in other regions (2–5 N_{Ex}/[kPa/year] and >3 N_{Ex}/kPa; Johnson et al., 2017a, 2017b, 2020; Xue et al., 2021). This reduced sensitivity may indicate that the long-term-averaged stressing rate in the inland Tohoku region is higher and the stress change perturbation (ratio of the seasonal stressing rate to the long-term-averaged stressing rate) is smaller than that in other regions, which is supported by the presence of strain concentration zones in the Niigata-Kobe Tectonic Zone and Ou Backbone Range (Miura et al., 2002, 2004; Sagiya et al., 2000). Another controlling factor may be that there are fewer crustal fluids to trigger seismicity in Japan (Brodsky et al., 2003; Harrington & Brodsky, 2006). Harrington and Brodsky (2006) found that the seismicity in Japan is less dynamically triggered by distant earthquakes than that in other regions; one possible mechanism for this reduced dynamic triggering is that the seismic waves from teleseismic earthquakes cannot unclog fluid-saturated crustal fractures, resulting in the relative inability of fluid infiltration into the surrounding pre-existing faults. The internal fluid pressure on the faults cannot increase because of frequent fracturing from nearby earthquakes before the fluids can saturate the cracks. This mechanism may be applicable where there are seasonal variations in seismicity if the fractures can be unclogged by the reduced surface loading, as opposed to the propagating seismic waves from teleseismic earthquakes.

4. Conclusions

We estimated the spatial distribution of the surface load using GNSS vertical displacement data from the inland Tohoku region and examined the relationship between subsurface stress changes induced by the estimated seasonal surface load and temporal trends in inland seismicity. The seasonal surface load increases in winter, decreases in spring, and is almost zero in summer and fall along the Sea of Japan. This seasonal surface load trend corresponds to the observed snow depth changes at the AMeDAS sites. Although we find a positive correlation between excess seismicity and stress changes, the seasonal modulation of seismicity is weaker than that observed in other regions. This might be due to the smaller perturbation of the stress changes relative to the long-term-averaged stressing rate and a relative inability to unclog the fluids in crustal fractures by reducing the surface load.

Data Availability Statement

The daily coordinate data of the GNSS stations are provided by the GSI (https://terras.gsi.go.jp/pos_main.php). The electronic reference point maintenance work list is available from GSI (https://terras.gsi.go.jp/denshi_hosyu.php). The elevation data is taken from NOAA National Centers for Environmental Information (2022). The JMA

10.1029/2023JB028217

catalog is produced by the JMA in cooperation with MEXT (Ministry of Education, Culture, Sports, Science and Technology) and is available from the NIED (National Research Institute for Earth Science and Disaster Resilience) Data Management Center (https://hinetwww11.bosai.go.jp/auth/JMA/?LANG=en; Login to the account is required). The source codes (FORTRAN) and manual for the HIST-ETAS model are available at Ogata et al. (2021). The maximum snow depth data are available from JMA (https://www.data.jma.go.jp/gmd/risk/obsdl/index.php). GRACE non tidal atmospheric geopotential coefficients are available at GRACE (2018). The Equivalent Water Height data derived from GRACE and GRACE-FO is available at Wiese et al. (2023). The figures were prepared using the Generic Mapping Tools software package (Wessel et al., 2019), which is available at https://www.generic-mapping-tools.org.

Acknowledgments
We are grateful to the Editor R. Abercrombie, the Associate Editor, and two reviewers J. Braunmiller and K. Heki for their useful comments. This study was supported by JSPS KAKENHI Grants 20J11654, 22KJ1770, 21H05205, and 18K03801. This research is a part of the PhD thesis of Taku Ueda (2022). CWJ is supported by the U.S. Department of Energy, Office of Science, Office of Basic Energy Sciences, Geosciences program under Award Number DE-FG02-09ERI6022.

References

Ader, T. J., Lapusta, N., Avouac, J. P., & Ampuero, J. P. (2014). Response of rate-and-state seismogenic faults to harmonic shear-stress perturbations. *Geophysical Jounral International*, *198*(1), 385–413. https://doi.org/10.1093/gji/ggu144

Akaike, H. (1980). Likelihood and the Bayes procedure. *Trabajos de Estadistica y de Investigacion Operativa*, *31*(1), 143–166. https://doi.org/10.1007/BF02888350

Amos, C. B., Audet, P., Hammond, W. C., Bürgmann, R., Johanson, I. A., & Blewitt, G. (2014). Uplift and seismicity driven by groundwater depletion in central California. *Nature*, *509*(7501), 483–486. https://doi.org/10.1038/nature13275

Bedford, J., & Bevis, M. (2018). Greedy automatic signal decomposition and its application to daily GPS time series. *Journal of Geophysical Research: Solid Earth*, *123*(8), 6992–7003. https://doi.org/10.1029/2017JB014765

Beeler, N. M., & Lockner, D. A. (2003). Why earthquakes correlate weakly with the solid Earth tides: Effects of periodic stress on the rate and probability of earthquake occurrence. *Journal of Geophysical Research*, *108*(B8), 2391. https://doi.org/10.1029/2001jb001518

Ben-Zion, Y., & Allam, A. A. (2013). Seasonal thermoelastic strain and postseismic effects in Parkfield borehole dilatometers. *Earth and Planetary Science Letters*, *379*, 120–126. https://doi.org/10.1016/j.epsl.2013.08.024

Bettinelli, P., Avouac, J. P., Flouzat, M., Bollinger, L., Ramillien, G., Rajaure, S., & Sapkota, S. (2008). Seasonal variations of seismicity and geodetic strain in the Himalaya induced by surface hydrology. *Earth and Planetary Science Letters*, *266*(3–4), 332–344. https://doi.org/10.1016/j.epsl.2007.11.021

Brodsky, E. E., Roeloffs, E., Woodcock, D., Gall, I., & Manga, M. (2003). A mechanism for sustained groundwater pressure changes induced by distant earthquakes. *Journal of Geophysical Research*, *108*(B8), 1–10. https://doi.org/10.1029/2002jb002321

Cleveland, R. B., Cleveland, W. S., McRae, J. E., & Terpenning, I. (1990). STL: A seasonal-trend decomposition procedure based on loess. *Journal of Official Statistics*, *6*(1), 3–73.

Cochran, E. S., Vidale, J. E., & Tanaka, S. (2004). Earth tides can trigger shallow thrust fault earthquakes. *Science*, *306*(5699), 1164–1166. https://doi.org/10.1126/science.1103961

Craig, T. J., Chanard, K., & Calais, E. (2017). Hydrologically-driven crustal stresses and seismicity in the New Madrid Seismic Zone. *Nature Communications*, *8*(2143), 1–11. https://doi.org/10.1038/s41467-017-01696-w

Dong, D., Fang, P., Bock, Y., Cheng, M. K., & Miyazaki, S. (2002). Anatomy of apparent seasonal variations from GPS-derived site position time series. *Journal of Geophysical Research*, *107*(B4), ETG9-1–ETG9-16. https://doi.org/10.1029/2001jb000573

Dong, D., Fang, P., Bock, Y., Webb, F., Prawirodirdjo, L., Kedar, S., & Jamason, P. (2006). Spatiotemporal filtering using principal component analysis and Karhunen-Loeve expansion approaches for regional GPS network analysis. *Journal of Geophysical Research*, *111*(3), 1–16. https://doi.org/10.1029/2005JB003806

Dziewonski, A. M., & Anderson, D. L. (1981). Preliminary reference Earth model. *Physics of the Earth and Planetary Interiors*, *25*(4), 297–356. https://doi.org/10.1016/0031-9201(81)90046-7

Fujiwara, S., Tobita, M., & Ozawa, S. (2022). Spatiotemporal functional modeling of postseismic deformations after the 2011 Tohoku-Oki earthquake. *Earth, Planets and Space*, *74*(13), 1–27. https://doi.org/10.1186/s40623-021-01568-0

Fukahata, Y., Nishitani, A., & Matsu'ura, M. (2004). Geodetic data inversion using ABIC to estimate slip history during one earthquake cycle with viscoelastic slip-response functions. *Geophysical Journal International*, *156*(1), 140–153. https://doi.org/10.1111/j.1365-246X.2004.02122.x

Gao, S. S., Silver, P. G., Llnde, A. T., & Sacks, I. S. (2000). Annual modulation of triggered seismicity following the 1992 Landers earthquake in California. *Nature*, *406*(6795), 500–504. https://doi.org/10.1038/35020045

GRACE. (2018). GRACE_GAA_L2_GRAV_GFZ_RL06. Ver. 6.0 [Dataset]. PO.DAAC. https://doi.org/10.5880/GFZ.GRACE_06_GAA

Hainzl, S., Ben-Zion, Y., Cattania, C., & Wassermann, J. (2013). Testing atmospheric and tidal earthquake triggering at Mt. Hochstaufen, Germany. *Journal of Geophysical Research: Solid Earth*, *118*(10), 5442–5452. https://doi.org/10.1002/jgrb.50387

Hainzl, S., Kraft, T., Wassermann, J., Igel, H., & Schmedes, E. (2006). Evidence for rainfall-triggered earthquake activity. *Geophysical Research Letters*, *33*(19), 1–5. https://doi.org/10.1029/2006GL027642

Harrington, R. M., & Brodsky, E. E. (2006). The absence of remotely triggered seismicity in Japan. *Bulletin of the Seismological Society of America*, *96*(3), 871–878. https://doi.org/10.1785/0120050076

Heki, K. (2001). Seasonal modulation of interseismic strain buildup in northeastern Japan driven by snow loads. *Science*, *293*(5527), 89–92. https://doi.org/10.1126/science.1061056

Heki, K. (2003). Snow load and seasonal variation of earthquake occurrence in Japan. *Earth and Planetary Science Letters*, *207*(1–4), 159–164. https://doi.org/10.1016/S0012-821X(02)01148-2

Heki, K. (2004). Dense GPS array as a new sensor of seasonal changes of surface loads. In R. S. J. Sparks & C. J. Hawkesworth (Eds.), *The state of the planet: Frontiers and challenges in geophysics, geophysical monograph series* (Vol. 150, pp. 177–196). American Geophysical Union.

Heki, K., & Jin, S. (2023). Geodetic studies on earth surface loading with GNSS and GRACE. *Satellite Navigation*, *4*(24), 1–13. https://doi.org/10.1186/s43020-023-00113-6

Hsu, Y., Kao, H., Bürgmann, R., Lee, Y., Huang, H., Hsu, Y., et al. (2021). Synchronized and asynchronous modulation of seismicity by hydrological loading: A case study in Taiwan. *Science Advances*, *7*(16), 1–12. https://doi.org/10.1126/sciadv.abf7282

Jaldehag, R. T. K., Johansson, J. M., Rönnäng, B. O., Elósegui, P., Davis, J. L., Shapiro, I. I., & Niell, A. E. (1996). Geodesy using the Swedish permanent GPS network: Effects of signal scattering on estimates of relative site positions. *Journal of Geophysical Research B: Solid Earth*, *101*(8), 17841–17860. https://doi.org/10.1029/96jb01183

Johnson, C. W., Fu, Y., & Bürgmann, R. (2017a). Seasonal water storage, stress modulation, and California seismicity. *Science*, *356*(6343), 1161–1164. https://doi.org/10.1126/science.aak9547

Johnson, C. W., Fu, Y., & Bürgmann, R. (2017b). Stress models of the annual hydrospheric, atmospheric, thermal, and tidal loading cycles on California faults: Perturbation of background stress and changes in seismicity. *Journal of Geophysical Research: Solid Earth*, *122*(12), 10605–10625. https://doi.org/10.1002/2017JB014778

Johnson, C. W., Fu, Y., & Bürgmann, R. (2020). Hydrospheric modulation of stress and seismicity on shallow faults in southern Alaska. *Earth and Planetary Science Letters*, *530*, 115904. https://doi.org/10.1016/j.epsl.2019.115904

Köhne, T., Riel, B., & Simons, M. (2023). Decomposition and inference of sources through spatiotemporal analysis of network signals: The DISSTANS Python package. *Computers and Geosciences*, *170*(October 2022), 105247. https://doi.org/10.1016/j.cageo.2022.105247

Kumazawa, T., & Ogata, Y. (2013). Quantitative description of induced seismic activity before and after the 2011 Tohoku-Oki earthquake by nonstationary ETAS models. *Journal of Geophysical Research: Solid Earth*, *118*(12), 6165–6182. https://doi.org/10.1002/2013JB010259

Larson, K. M. (2013). A methodology to eliminate snow- and ice-contaminated solutions from GPS coordinate time series. *Journal of Geophysical Research: Solid Earth*, *118*(8), 4503–4510. https://doi.org/10.1002/jgrb.50307

Larson, K. M., Wahr, J., & Kuipers Munneke, P. (2015). Constraints on snow accumulation and firn density in Greenland using GPS receivers. *Jounral of Glaciology*, *61*(225), 101–114. https://doi.org/10.3189/2015JoG14J130

Miura, S., Sato, T., Hasegawa, A., Suwa, Y., Tachibana, K., & Yui, S. (2004). Strain concentration zone along the volcanic front derived by GPS observations in NE Japan arc. *Earth, Planets and Space*, *56*(12), 1347–1355. https://doi.org/10.1186/BF03353360

Miura, S., Sato, T., Tachibana, K., Satake, Y., & Hasegawa, A. (2002). Strain accumulation in and around Ou Backbone Range, northeastern Japan as observed by a dense GPS network. *Earth, Planets and Space*, *54*(11), 1071–1076. https://doi.org/10.1186/BF03353304

Morishita, Y., Lazecky, M., Wright, T. J., Weiss, J. R., Elliott, J. R., & Hooper, A. (2020). LiCSBAS: An open-source InSAR time series analysis package integrated with the LiCSAR automated sentinel-1 InSAR processor. *Remote Sensing*, *12*(424), 1–29. https://doi.org/10.3390/rs12030424

Munekane, H., Tobita, M., & Takashima, K. (2004). Groundwater-induced vertical movements observed in Tsukuba, Japan. *Geophysical Research Letters*, *31*(12), 2–5. https://doi.org/10.1029/2004GL020158

NOAA National Centers for Environmental Information. (2022). ETOPO 2022 15 arc-second global relief model [Dataset]. NOAA National Centers for Environmental Information. https://doi.org/10.25921/fd45-gt74

Ogata, Y. (2004). Space-time model for regional seismicity and detection of crustal stress changes. *Journal of Geophysical Research*, *109*(B3), B03308. https://doi.org/10.1029/2003jb002621

Ogata, Y., Katsura, K., & Tanemura, M. (2003). Modelling heterogeneous space-time occurrences of earthquakes and its residual analysis. *Journal of the Royal Statistical Society. Series C (Applied Statistics)*, *52*(4), 499–509. https://doi.org/10.1111/1467-9876.00420

Ogata, Y., Katsura, K., Tanemura, M., Harte, D., & Zhuang, J. (2021). Hierarchical space-time point-process models (HIST-PPM): Software documentation and codes [Software]. Computer Science Monograph 35. Retrieved from https://www.ism.ac.jp/editsec/csm/index.html

Okada, M. (1982). Seasonal variation in the occurrence rate of large earthquakes in and near Japan and its regional differences. *Zisin (Journal of the Seismological Society of Japan. 2nd Series)*, *35*(1), 53–64. https://doi.org/10.4294/zisin1948.35.1_53

Okada, Y. (1995). Simulated empirical law of coseismic crustal deformation. *Journal of Physics of the Earth*, *43*(6), 697–713. https://doi.org/10.4294/jpe1952.43.697

Pollitz, F. F. (1996). Coseismic deformation from earthquake faulting on a layered spherical earth. *Geophysical Journal International*, *125*, 1–14. https://doi.org/10.1111/j.1365-246x.1996.tb06530.x

Pollitz, F. F., Wech, A., Kao, H., & Bürgmann, R. (2013). Annual modulation of non-volcanic tremor in northern Cascadia. *Journal of Geophysical Research: Solid Earth*, *118*(5), 2445–2459. https://doi.org/10.1002/jgrb.50181

Sagiya, T., Miyazaki, S., & Tada, T. (2000). Continuous GPS array and present-day crustal deformation of Japan. *Pure and Applied Geophysics*, *157*(11–12), 2303–2322. https://doi.org/10.1007/978-3-0348-7695-7_26

Sato, H. P., Abe, K., & Ootaki, O. (2003). GPS-measured land subsidence in Ojiya City, Niigata Prefecture, Japan. *Engineering Geology*, *67*(3–4), 379–390. https://doi.org/10.1016/S0013-7952(02)00221-1

Schuster, A. (1897). On lunar and solar periodicities of earthquakes. *Proceedings of the Royal Society of London*, *61*, 455–465.

She, Y., Fu, G., & Xu, C. (2022). Seasonal terrestrial water load modulation of seismicity at the southeastern margin of the Tibetan Plateau constrained by GNSS and GRACE data. *Geophysical Journal International*, *230*(3), 1966–1979. https://doi.org/10.1093/gji/ggac168

Shimada, S., Aichi, M., Harada, T., & Tokunaga, T. (2021). Time variations of the vertical component in some of Japanese GEONET GNSS sites. In *International Association of Geodesy Symposia* (pp. 1–8). https://doi.org/10.1007/1345_2021_135

Takamatsu, N., Muramatsu, H., Abe, S., Hatanaka, Y., Furuya, T., Kakiage, Y., et al. (2023). New GEONET analysis strategy at GSI: Daily coordinates of over 1300 GNSS CORS in Japan throughout the last quarter century. *Earth, Planets and Space*, *75*(1), 49. https://doi.org/10.1186/s40623-023-01787-7

Terakawa, T., & Matsu'ura, M. (2008). CMT data inversion using a Bayesian information criterion to estimate seismogenic stress fields. *Geophysical Journal International*, *172*(2), 674–685. https://doi.org/10.1111/j.1365-246X.2007.03656.x

Terakawa, T., & Matsu'ura, M. (2010). The 3-D tectonic stress fields in and around Japan inverted from centroid moment tensor data of seismic events. *Tectonics*, *29*(6), 1–14. https://doi.org/10.1029/2009TC002626

Tobita, M., Munekane, H., Kaidzu, M., Matsuzaka, S., Kuroishi, Y., Masaki, Y., & Kato, M. (2004). Seasonal variation of groundwater level and ground level around Tsukuba. *Journal of the Geodetic Society of Japan*, *50*(1), 27–37.

Tsuruoka, H., Ohtake, M., & Sato, H. (1995). Statistical test of the tidal triggering of earthquakes: Contribution of the ocean tide loading effect. *Geophysical Journal International*, *122*(1), 183–194. https://doi.org/10.1111/j.1365-246X.1995.tb03546.x

Ueda, T. (2022). Seismicity analysis based on statistical modeling: Connection with stress change (Doctoral dissertation). The University of Tokyo.

Ueda, T., & Kato, A. (2019). Seasonal variations in crustal seismicity in San-in District, Southwest Japan. *Geophysical Research Letters*, *46*(6), 3172–3179. https://doi.org/10.1029/2018GL081789

Ueda, T., & Kato, A. (2023). Aftershocks following the 2011 Tohoku-Oki earthquake driven by both stress transfer and afterslip. *Progress in Earth and Planetary Science*, *10*(1), 31. https://doi.org/10.1186/s40645-023-00564-0

Ueda, T., Kato, A., Ogata, Y., & Yamaya, L. (2021). Spatial variations in seismicity characteristics in and around the source region of the 2019 Yamagata-Oki Earthquake, Japan. *Earth, Planets and Space*, *73*(40), 1–10. https://doi.org/10.21203/rs.3.rs-34752/v1

Wahr, J., Khan, S. A., Van Dam, T., Liu, L., Van Angelen, J. H., Van Den Broeke, M. R., & Meertens, C. M. (2013). The use of GPS horizontals for loading studies, with applications to northern California and southeast Greenland. *Journal of Geophysical Research: Solid Earth*, *118*(4), 1795–1806. https://doi.org/10.1002/jgrb.50104

Wang, H., Xiang, L., Jia, L., Jiang, L., Wang, Z., Hu, B., & Gao, P. (2012). Load Love numbers and Green's functions for elastic Earth models PREM, iasp91, ak135, and modified models with refined crustal structure from Crust 2.0. *Computers and Geosciences*, *49*, 190–199. https://doi.org/10.1016/j.cageo.2012.06.022

Wessel, P., Luis, J. F., Uieda, L., Scharroo, R., Wobbe, F., Smith, W. H. F., & Tian, D. (2019). The Generic Mapping Tools Version 6. *Geochemistry, Geophysics, Geosystems*, *20*(11), 5556–5564. https://doi.org/10.1029/2019GC008515

Wiemer, S., & Wyss (2000). Minimum magnitude of completeness in earthquake catalogs: Examples from Alaska, the western United States, and Japan. *Bulletin of the Seismological Society of America*, *90*(4), 859–869. https://doi.org/10.1785/0119990114

Wiese, D. N., Yuan, D.-N., Boening, C., Landerer, F. W., & Watkins, M. M. (2023). JPL GRACE and GRACE-FO Mascon Ocean, ice, and hydrology equivalent water height CRI filtered. Ver. RL06.1Mv03 [Dataset]. PO.DAAC. https://doi.org/10.5067/TEMSC-3JC63

Xue, L., Fu, Y., Johnson, C. W., Otero Torres, J. J., Shum, C. K., & Bürgmann, R. (2021). Seasonal seismicity in the Lake Biwa Region of Central Japan moderately modulated by lake water storage changes. *Journal of Geophysical Research: Solid Earth*, *126*(12), e2021JB023301. https://doi.org/10.1029/2021jb023301

Xue, L., Johnson, C. W., Fu, Y., & Bürgmann, R. (2020). Seasonal seismicity in the western branch of the east African rift system. *Geophysical Research Letters*, *47*(6), 1–9. https://doi.org/10.1029/2019GL085882

Yao, D., Huang, Y., Xue, L., Fu, Y., Gronewold, A., & Fox, J. L. (2022). Seismicity around Southern Lake Erie during 2013 – 2020 in relation to lake water level. *Seismological Research Letters*, *93*(4), 2268–2280. https://doi.org/10.1785/0220210343

Zhang, L., Tang, H., & Sun, W. (2021). Comparison of GRACE and GNSS seasonal load displacements considering regional averages and discrete points. *Journal of Geophysical Research: Solid Earth*, *126*(8), e2021JB021775. https://doi.org/10.1029/2021JB021775

Zhuang, J., Ogata, Y., & Vere-jones, D. (2002). Stochastic declustering of space-time earthquake occurrences. *Journal of the American Statistical Association*, *97*(458), 369–380. https://doi.org/10.1198/016214502760046925